

Voltage Feasibility Boundaries for Power System Security Assessment

Mazhar Ali, Elena Gryazina, Anatoly Dymarsky, and Petr Vorobev, *Member IEEE*

Abstract—Modern power systems face a grand challenge in grid management due to increased electricity demand, imminent disturbances, and uncertainties associated with renewable generation, which can compromise grid security. The security assessment is directly connected to the robustness of the operating condition and is evaluated by analyzing proximity to the power flow solution space’s boundary. Calculating location of such a boundary is a computationally challenging task, linked to the power flow equations’ non-linear nature, presence of technological constraints, and complicated network topology. In this paper we introduce a general framework to characterize points on the power flow solution space boundary in terms of auxiliary variables subject to algebraic constraints. Then we develop an adaptive continuation algorithm to trace 1-dimensional sections of boundary curves which exhibits robust performance and computational tractability. Implementation of the algorithm is described in detail, and its performance is validated on different test networks.

Index Terms—Power system security assessment, Voltage feasibility space, Continuation methods.

I. INTRODUCTION

Power system security has always been a subject of paramount importance as electric grids transform into convoluted structures to address the growing electricity demand [1]. Furthermore, integration of Distributed Energy Resources (DERs) like wind turbines, photovoltaics, or other renewables has introduced an abstruse uncertainty in the grid’s operation, begetting tremendous concern for its stability. Hence, the security assessment is crucial to ensure secure and economical operation by evaluating operational state robustness against potential contingencies [1]. It has, consequently, been approached by analyzing the boundaries of the power flow solution map.

Power flow solution boundaries separate regions in the parameter space corresponding to the existence of real-valued solution of the power flow equations. [2]. Quantifying boundary curves is indispensable for planning and operational purposes to reduce the risk of disruption, optimize the power transfers, and take full advantage of the transmission capabilities [3]. Also, to expedite the decision-making process to maintain the power system security and price stability [4], [5].

Mathematically, points on the solution space boundary satisfy the power flow equations’ real-valued solution, and the degenerate condition of the power flow Jacobian (referred to as “Transversality” condition) [2], [4]. These conditions describe the boundary of solvability region. To calculate the feasibility space boundary, the operational inequalities like limits on voltage setpoints, transmission line thermal limits, and generator power outputs, etc., must be valid along with the conditions stated earlier. This paper aims to investigate the feasibility boundary of the power flow equations.

In early studies, the power flow solution space structure was hypothesized as convex [6]. However, an example from [4]

represents a non-convex topology with inner folds, manifesting multiple equilibria regions. This embedded complexity within the power flow solution space makes calculating its boundary a challenging task from the computational context. The past contributions fall into two main categories. The first type focuses on calculating only a single point on the power flow solution boundary. They include Continuation Power Flow (CPF) approaches [7], [8], direct methods from [9], nonlinear programming techniques from [10], [11], and some recently published innovative algorithms as described in [12].

The second category of efforts investigates the power flow solution’s boundary in the multi-dimensional space. Only a handful of steps are made in this direction. The most notable work from [4] introduces a Predictor-Corrector (PC) continuation method to compute the solution space boundary nomograms. It uses tangents as predictors and hyperplanes as correctors. Such homotopy path tracking routines have a difficult implementation and exhibit slow convergence for tracing curves with sharp edges, or non-convexities [13]. Also, the formulation in [4] uses a right eigenvector transversality condition to enforce the non-trivial kernel of the power flow Jacobian, and it doubles the number of system variables. Hence, resulting in an additional computational burden. This condition also makes the initialization of the continuation procedure sensitive to a good guess of the right eigenvector. Moreover, the formulation from [4] does not consider any operational inequalities. Therefore, it is confined to study only the solvability space of the power flow equations.

An alternative approach to study the boundary of the power flow solution space was made by the Numerical Polynomial Homotopy Continuation (NPHC) method. The contributions from [14] and [15] show an implementation of NPHC method to compute the power flow equations’ feasibility space. The inherent mathematical framework of the NPHC algorithm guarantees to find all isolated solutions of the power flow equations. It uses a PC continuation scheme to trace all these solutions along with a one-dimensional parametrization. Despite the computational robustness, the NPHC algorithm suffers from a large computational overhead as it employs numerous continuation traces to determine all solutions.

Past contributions are mostly focused on the study of only solvability space, i.e., without considering technological constraints. This manuscript aims to compute the power flow feasibility boundary with computational tractability, speed, and scalability to large networks. The key contributions of this paper are as follow:

- I. A general mathematical structure is proposed to extend the problem from solvability space towards the boundary

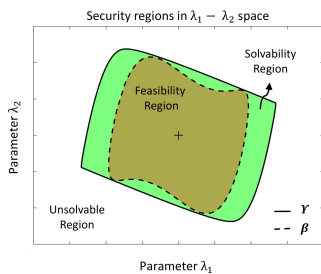


Fig. 1: Steady-state security regions in $\lambda_1 - \lambda_2$ space (varying parameters, like power injections, voltage setpoints, etc.).

of feasibility space by a set of complementary equations representing the operational inequalities.

- II. Compared to the eigenvector based transversality condition, a scalar transversality condition is used to characterize points on the solution space boundary. It results in a small computational overhead, does not suffer from initialization issues, and provides better scalability for large networks.
- III. This paper introduces the use of a Homotopy Continuation Method (HCM) referred to as ‘‘Spherical Continuation’’, which allows tracing the solution curves with sharp edges or non-convexities. An adaptive sphere size approach further improves the robustness and speed of this algorithm.

II. PROBLEM STATEMENT

Here, Figure.1 depicts steady-state security regions such as feasibility, solvability, and unsolvable regions to illustrate the importance of the power flow solution map’s boundedness in conjunction with the power system security assessment.

First, the feasibility region describes the set of operating points for which the real-valued solution to power flow equations exists. The operational constraints like limits on voltage setpoints, generator power outputs, etc., are also satisfied. Usually, this is the optimal operating region for a grid. It is enclosed by a curve ‘‘ β ’’ referred to as the voltage feasibility or just feasibility boundary. Secondly, the solvability region contains operating points for which the real-valued solution to the power flow equations still exists, but one or more operational constraints may be violated. The operation is still possible in this domain, but tractable measures must bring the operating point back to the feasible space. This region’s boundary is outlined by ‘‘ γ ’’ curve and generally known as the solvability boundary. Finally, the area outside the solvability space is an unsolvable region, as the real-valued solution to the power flow equations disappears. Any operation in this space will result in system instability or voltage collapse.

The quantification of the power flow solution boundaries (i.e., γ and β curves) can help Transmission System Operator (TSO) in security assessment by; i) determining the relative degree of security for a given operating state. ii) providing acceptable maneuverability for a continuously moving operating regime, iii) help decide optimum control actions to bring the operational state back to the feasible domain.

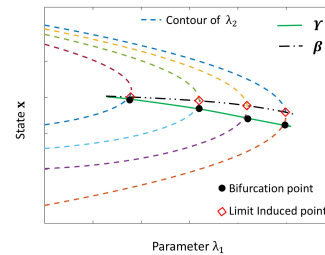


Fig. 2: Power flow solution space boundaries in $\lambda_1 - \lambda_2$ space.

A. Mathematical Formulation

We can describe the power flow problem with the following compact notation,

$$\mathcal{F}(\mathbf{x}, \lambda) = \mathbf{0} \quad (1)$$

Here, $\mathcal{F}(\mathbf{x}, \lambda) : \mathbb{R}^n \times \mathbb{R}^p \rightarrow \mathbb{R}^n$ constitute ‘‘ n ’’ number of nonlinear algebraic equations including both the power flows and the technological constraints, $\mathbf{x} \in \mathbb{R}^n$ is a vector of system variables (like voltage magnitudes and phase angles), while $\lambda \in \mathbb{R}^p$ are the system parameters (like limits on the nodal power injections, or limits on the line currents etc.).

a) *Solution space*: The system in (1) describes n -number of equations in $(n + p)$ variables. For ‘‘ p ’’ free varying parameters the solution space of (1) defines a p -dimensional manifold. Let $p = 1$, solution of (1) delineate 1-dimensional curves. For example, dashed curves in Fig.2 represents solution of system in (1) by releasing a single parameter λ_1 , i.e., injected power while observing the state variable \mathbf{x} like voltage magnitudes. These curves are analogous to PV or ‘‘nose curves’’ of the power flow problem. If another parameter λ_2 is also free to vary then the solution space of (1) is a 2-dimensional surface, dashed curves in Fig.2 are contours of such surface.

b) *Solution space boundary*: This work aims to construct the boundary of the solution space of (1). Such boundary defines the boundedness of the power flow solution space. At any point on this boundary, the real-valued solution for the system in (1) disappears either due to the unsolvability of power flow equations or due to the violation of some operational constraints. Mathematically, this condition can be enforced as,

$$g(\mathbf{x}) = \det \nabla_{\mathbf{x}} \mathcal{F}(\mathbf{x}, \lambda) = 0. \quad (2)$$

Here (2) is referred to as transversality condition [9] corresponding to the degeneracy of the $n \times n$ power flow Jacobian matrix $\nabla_{\mathbf{x}} \mathcal{F}$. There are several ways to enforce (2), more details are given in the subsequent section.

Introducing (2) along with (1), makes the number of equations $(n + 1)$ in $(n + p)$ variables. Following the same generalization, for ‘‘ p ’’ free varying parameters the solution space boundary of (1) will be a $(p - 1)$ -dimensional manifold in the parameter space of λ ’s. If we consider $p = 1$ then we have $(n + 1)$ equations in $(n + 1)$ variables and solution of (1) together with (2) is just a single point on the solution space boundary. In Fig.2 these boundary points are shown on both solvability boundary curve γ and also on the feasibility boundary β . To

sum up, the problem formulation for calculating the boundary of power flow solution space is described by solving the set of equations in (1) along with condition (2). The true solution boundary is a multi-dimensional hypersurface. Therefore, it is computationally infeasible to construct even for reasonably small networks. However, calculating a 1-dimensional slice of this high-dimensional hypersurface is computationally tractable and does provide a reliable way to assess the grid's security. The context of this work examines the structure of the solution boundary with $p = 2$ resulting in a 1-dimensional boundary curves. The examples in Section.IV also show a 2-dimensional solution boundary surface (i.e., for $p = 3$).

B. System of Equations and Variables

In this section we describe the system of equations and variables considered in $\mathcal{F}(\mathbf{x}, \lambda) = \mathbf{0}$.

1) *Modeling Power Flows*: Here, a rectangular formulation is adopted for the power flow model. Let us consider the real representation of the power flow equations in terms of the real and imaginary part of the complex voltage phasor $\hat{V}_i \in \mathbb{C}^n$ as $\hat{V}_i = V_i^r + \mathbf{j}V_i^m$. Let n be the total number of buses in the network with $\mathcal{N} = \{1, 2, \dots, n\}$ representing the set of all buses, while \mathcal{L} is the set of load buses (PQ), and \mathcal{G} is the set of generator buses (PV). For each bus, $i \in \mathcal{N}$ except the slack bus, the active power balance can be stated as,

$$\sum_k \left\{ V_i^r (G_{ik} V_k^r - B_{ik} V_k^m) + V_i^m (G_{ik} V_k^m + B_{ik} V_k^r) \right\} - \lambda (P_i^{\text{gen}} - P_i^{\text{load}}) = 0. \quad (3)$$

Similarly, the reactive power balance at each load bus $i \in \mathcal{L}$ can be defined as,

$$\sum_k \left\{ V_i^m (G_{ik} V_k^r - B_{ik} V_k^m) - V_i^r (G_{ik} V_k^m + B_{ik} V_k^r) \right\} - \lambda (Q_i^{\text{gen}} - Q_i^{\text{load}}) = 0. \quad (4)$$

The parameter λ represents the boundness of the nodal power injections, while subscripts "gen" and "load" express bus loading and generation levels. In (3) and (4) G_{ij} and B_{ij} denote the real and imaginary entries of the complex admittance matrix $\hat{Y}_{ij} = G_{ij} + \mathbf{j}B_{ij}$. For each generator, $i \in \mathcal{G}$ the fixed voltage levels are characterized by an additional equation,

$$(V_i^r)^2 + (V_i^m)^2 - |\hat{V}_i|_{\text{ref}}^2 = 0. \quad (5)$$

In (5) $|\hat{V}_i|_{\text{ref}}$ is the specified voltage magnitude at the i^{th} generator bus.

2) *Voltage magnitude limits*: If the system in (1) considers only the power flow equations i.e., (3), (4) and (5), then the problem formulation is limited to the boundary of the solvability space. Typically, a real power system is operated with technological constraints. Usually, these constraints are given in the form of inequalities with maximum and minimum bounds. To extend the problem to the boundary of the feasibility space (i.e., β curve from Fig.11), we reformulate inequality constraints into a set of polynomial equations suitable to consider in (1). For example, at each load bus $i \in \mathcal{L}$, voltage magnitudes are given within specified bounds as,

$$|\hat{V}_i|_{\min} \leq |V_i|_{\text{cal}} \leq |\hat{V}_i|_{\max} \quad (6)$$

Here $|V_i|_{\text{cal}}$ specifies the calculated voltage magnitude level. While $|\hat{V}_i|_{\max}$ and $|\hat{V}_i|_{\min}$ represent maximum and minimum bound on the voltage magnitude. To have a solvable solution of (6), slack variables were introduced to convert this inequality constraint into two different equality equations corresponding to $|\hat{V}_i|_{\max}$ and $|\hat{V}_i|_{\min}$ respectively,

$$(V_i^r)^2 + (V_i^m)^2 - |\hat{V}_i|_{\max}^2 + (\bar{s}_i)^2 = 0 \quad (7a)$$

$$(V_i^r)^2 + (V_i^m)^2 - |\hat{V}_i|_{\min}^2 - (\underline{s}_i)^2 = 0 \quad (7b)$$

In (7), \bar{s}_i and \underline{s}_i denote the slack variables related to each limit. From (7), one can conclude that the real solution for slack variables \bar{s}_i and \underline{s}_i exists only if voltage levels lie within acceptable limits, and vice-versa, such a solution does not exist if the limits are violated. Thus, we have reduced the feasibility problem to the solvability problem of a certain equivalent system.

Here, we consider the constraints of the type (6), however any other constraints like limits on generator power outputs or transmission line thermal limits can be reformulated using the same slack variable methodology [16] similarly to (7). It is worth noticing that even with additional equations, the given methodology preserves the power flow model's sparsity characteristics. To summarize, the system in (1) considers equations, (3), (4), (7a), and (7b) for every PQ bus, while two equations - (4) and (5) - are defined for every PV bus. The variable vector \mathbf{x} contains n components, namely variables $V_i^r, V_i^m, \bar{s}_i, \underline{s}_i$ for every PQ bus and variables V_i^r, V_i^m for every PV bus.

III. PROPOSED METHODOLOGY

In the present section, we first outline the choice of transversality condition $g(\mathbf{x})$ followed by the discussion of the proposed algorithm.

A. Transversality condition $g(\mathbf{x})$

Normally, the transversality condition is applied using the determinant as in (2). It is simple to implement but suffers from a high computational burden, numerical stability issues, and poor scalability to larger networks. The conventional way to enforce this condition uses a right eigenvector corresponding to the null space of $\nabla_{\mathbf{x}} \mathcal{F}(\mathbf{x}, \lambda)$ as,

$$g_{\text{eig}}(\mathbf{x}, \mathbf{y}) = \left[\frac{\nabla_{\mathbf{x}} \mathcal{F}(\mathbf{x}, \lambda) \cdot \mathbf{y}}{\mathbf{y}^T \mathbf{y} - 1} \right] = \mathbf{0}. \quad (8)$$

In (8) \mathbf{y} is a normalised eigenvector corresponding to zero eigenvalue of $\nabla_{\mathbf{x}} \mathcal{F}(\mathbf{x}, \lambda)$. Introducing $g(\mathbf{x})$ through (8) has the benefit of preserving the power flow problem's sparsity structure. But, the convergence is sensitive to a good initial guess of the eigenvector \mathbf{y} and displays poor scalability as dimension of system variables increases by a factor of two.

Several choices of $g(\mathbf{x})$ are explored in [9] with fast algorithms to evaluate their gradients. We employ a scalar transversality condition based on the Singular Value Decomposition (SVD) due to the small computational cost, numerical stability, and scalability to large networks. Let the SVD of the $n \times n$ Jacobian matrix \mathbf{J} i.e., $\nabla_{\mathbf{x}} \mathcal{F}(\mathbf{x}, \lambda)$ be,

$$\mathbf{J} = \mathbf{U} \mathbf{\Sigma} \mathbf{V}^T = \sum_{i=1}^n \sigma_i \mathbf{u}_i \mathbf{v}_i^T. \quad (9)$$

Here \mathbf{U} and \mathbf{V} are the orthogonal matrices with same dimensions as \mathbf{J} , while $\mathbf{\Sigma}$ is a diagonal matrix consisting of singular values such that $\sigma_i \geq 0$, $i = 1, 2, \dots, n$. At the solution boundary the Jacobin becomes singular, thus the minimum singular value of \mathbf{J} becomes equal to zero i.e., $\sigma_{nm} = 0$. Consequently, one can enforce the following necessary condition for characterizing the solution of (1) on the feasibility boundary,

$$g_{\text{svd}}(\mathbf{x}) = \mathbf{u}_n^\top \mathbf{J} \mathbf{v}_n = 0. \quad (10)$$

Here, \mathbf{u}_n and \mathbf{v}_n correspond to the n^{th} left and right singular vectors. Introducing $g(\mathbf{x})$ by (10) has following advantages over (8); i) small computational overhead as only one additional variable is introduced, ii) does not require any guess for initialization compared to g_{eig} , iii) the singular values are less sensitive to numerical perturbations. iv) finally, better scalability as this condition requires computing SVD only for the lowest singular value, which can be performed with a breakneck speed for sparse structured matrices like Jacobian \mathbf{J} . One can now describe the solution of system in (1) on the boundary by enforcing condition (10).

B. Homotopy Continuation Method

The general set of equations defining the points on the boundary of the power flow solution space can be stated as,

$$\mathcal{H}(\mathbf{z}) = \mathbf{0}. \quad (11)$$

Where,

$$\mathcal{H}(\mathbf{z}) = \begin{bmatrix} \mathcal{F}(\mathbf{x}, \lambda) \\ g_{\text{svd}}(\mathbf{x}) \end{bmatrix} \in \mathbb{R}^{n+1}, \quad \mathbf{z} = \begin{bmatrix} \mathbf{x} \\ \lambda \end{bmatrix} \in \mathbb{R}^{n+p} \quad (12)$$

Using the same generalization, if there are “ p ” free varying parameters i.e., $\lambda \in \mathbb{R}^p$, the solution of (11) corresponds to a $(p - 1)$ -dimensional manifold. This paper considers formulation with $p = 2$ resulting in a curve or 1-dimensional curve of solution points.

Generally, Homotopy Continuation Methods (HCMs) are deployed for tracing solution curves, with some suitable path-tracking algorithms. Namely, i) Euler Homotopy or Predictor-Corrector (PC) algorithms, and ii) Simplicial Continuation or Piecewise-Linear (PL) algorithms [13], [17]. Here, we describe a PC algorithm to trace the homotopy path, as the underlying equations in (11) represent a smooth map. The PC algorithms are also more efficient in higher-dimensional cases compared to the PL algorithms. Conventionally, the PC algorithms apply tangents as predictors and hyperplanes as correctors (like in [4]). Such an algorithmic routine suffers from difficult implementation, convergence issues, and manifest slow performance in the vicinity of sharp turning points or non-convex sections of the solution curve [13]. This paper implements an adaptive Spherical Continuation (SC) algorithm for curve tracing using spheres, with a precise geometrical description, ease of implementation, and computational tractability.

1) *Spherical Continuation Path Tracking*: Let us consider a sphere “ s_1 ” of radius “ r ” as shown in Fig.3, centered at \mathbf{z}_1 on the homotopy path “ β ” defined by (11). Its outline must intersect the homotopy curve at least at two possible

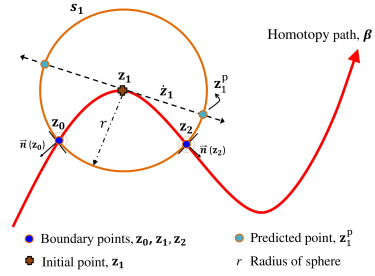


Fig. 3: Intersection of sphere s_1 with a homotopy path β .

points, one in the forward direction “ z_0 ”, and another one in the backward direction “ z_2 ”. The given formulation of the homotopy system (11) has $(n + 1)$ equations in $(n + 2)$ variables, it means that we should include an additional equation representing a $(n + 2)$ -dimensional hypersphere to trace the homotopy path. Thus, the equation of the hypersphere intersecting the homotopy path β can be introduced as,

$$\mathcal{S}(\mathbf{z}, r) = \sum_m^{n+2} (\mathbf{z}^m - \mathbf{z}_1^m)^2 - r^2 = 0. \quad (13)$$

Figure (4) shows the Spherical path tracking of the homotopy curve β . To trace the succeeding points, i.e., $\mathbf{z}_2, \mathbf{z}_3, \dots$ on the homotopy curve, the PC algorithm starts from an Euler Predictor followed by a Generalized Newton-Raphson Corrector.

a) *Euler predictor*: The algorithm is driven from an initial point \mathbf{z}_1 on the β curve that satisfies $\mathcal{H}(\mathbf{z}_1) = 0$. To compute the next point \mathbf{z}_2 on the curve, first a predictor point \mathbf{z}_1^p is calculated on the sphere s_1 through an Euler predictor.

Let us assume an arc-length parametrization “ α ” of the homotopy curve β is a smooth function $\mathbf{z}(\alpha) : \mathbb{R}^+ \rightarrow \beta$ such that $\mathbf{z}(0) = \mathbf{z}_1$, and $\mathcal{H}(\mathbf{z}(\alpha)) = 0$. The tangent vector $\dot{\mathbf{z}}(\alpha)$ always has a unit length for all $\alpha \in \mathbb{R}^+$. The aforementioned conditions for $\mathbf{z}(\alpha)$ make it a solution of the following system of differential equations,

$$\nabla_{\mathbf{z}} \mathcal{H}(\mathbf{z}(\alpha)) \cdot \dot{\mathbf{z}}(\alpha) = \mathbf{0} \quad (14a)$$

$$\dot{\mathbf{z}}(\alpha)^\top \cdot \dot{\mathbf{z}}(\alpha) = 1. \quad (14b)$$

$$\mathbf{z}(0) = \mathbf{z}_1 \quad (14c)$$

Where $\nabla_{\mathbf{z}} \mathcal{H}(\mathbf{z}(\alpha))$ is the $(n + 1) \times (n + 2)$ Jacobian matrix and has a rank $(n + 1)$ by assumption. While $\dot{\mathbf{z}}(\alpha)$ is the normalized tangent vector spanning the one-dimensional kernel $\ker(\nabla_{\mathbf{z}} \mathcal{H}(\mathbf{z}(\alpha)))$. From (14) it is clear that the kernel of the Jacobian $\nabla_{\mathbf{z}} \mathcal{H}(\mathbf{z}(\alpha))$ has two vectors of unit norm which correspond to the two possible directions of traversing the β curve (see Fig.3). To specify the direction in which the curve is traversed following condition is introduced along with (14)

$$\det \begin{pmatrix} \nabla_{\mathbf{z}} \mathcal{H}(\mathbf{z}(\alpha)) \\ \dot{\mathbf{z}}(\alpha)^\top \end{pmatrix} > 0 \quad (15)$$

The tangent vector $\dot{\mathbf{z}}(\alpha)$ can be calculated numerically via SVD decomposition if,

$$\left. \left(\nabla_{\mathbf{z}} \mathcal{H}(\mathbf{z}) \right)^\top \right|_{\mathbf{z}=\mathbf{z}_1} = \mathbf{M} \begin{pmatrix} \mathbf{D} \\ \mathbf{0} \end{pmatrix} \mathbf{N}^\top. \quad (16)$$

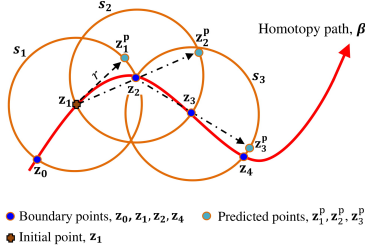


Fig. 4: Spherical continuation, path tracking procedure.

Here \mathbf{M} is a $(n+2) \times (n+2)$ left orthogonal matrix composed of $(n+2)$ orthonormal vectors $\mathbf{M} = [\mathbf{m}_1, \mathbf{m}_2, \dots, \mathbf{m}_{n+2}]$, and \mathbf{D} is a $(n+1) \times (n+1)$ full rank diagonal matrix consisting of $(n+1)$ singular values. While \mathbf{N} is a $(n+1) \times (n+1)$ right orthogonal matrix composed of $(n+1)$ orthonormal vectors $\mathbf{N} = [\mathbf{n}_1, \mathbf{n}_2, \dots, \mathbf{n}_{n+1}]$. After some algebraic manipulation, the expression in (16) can be stated as,

$$\nabla_{\mathbf{z}} \mathcal{H}(\mathbf{z})|_{\mathbf{z}=\mathbf{z}_1} \mathbf{M} = \mathbf{N} \begin{pmatrix} \mathbf{D} & \mathbf{0} \end{pmatrix}. \quad (17)$$

Let $\delta \mathbf{z}$ is the n^{th} orthonormal vector such that $\delta \mathbf{z} = \mathbf{m}_{n+2} = \mathbf{M} \cdot \mathbf{e}_{n+2}$ (with $\mathbf{e}_{n+2} = (0, \dots, 0, 1)^\top \in \mathbb{R}^{n+2}$) such that:

$$\nabla_{\mathbf{z}} \mathcal{H}(\mathbf{z})|_{\mathbf{z}=\mathbf{z}_1} \cdot \delta \mathbf{z} = \mathbf{0} \quad (18a)$$

$$\delta \mathbf{z}^\top \cdot \delta \mathbf{z} = 1. \quad (18b)$$

Condition (15) for traversing the curve in a forward direction can be interpreted by the sign of the $(\det(\mathbf{M}) \cdot \det(\mathbf{D}) \cdot \det(\mathbf{N}))$, which can be computed without any additional computational cost. Finally, the predicted point on the sphere s_1 with radius r is given by,

$$\mathbf{z}_1^p = \mathbf{z}_1 + r \cdot \delta \mathbf{z} \quad (19)$$

b) Generalized Newton Corrector: The predicted solution \mathbf{z}_1^p is just an estimate of the actual point on the curve. Hence, a correction step is essential to calculate an exact point on the curve. The subsequent set of equations are solved in the corrector step to calculate a forward solution \mathbf{z}_2 on the homotopy path,

$$\mathcal{H}(\mathbf{z}) = \mathbf{0}, \quad (20a)$$

$$\mathcal{S}(\mathbf{z}, r) = \sum_m^{n+2} (\mathbf{z}^m - \mathbf{z}_1^m)^2 - r^2 = 0. \quad (20b)$$

The system in (20) forms a set of $(n+2)$ equations in $(n+2)$ unknowns, which can be solved using any standard technique, such as Newton-Raphson. Linearizing (20) at \mathbf{z}_1^p by first order Taylor series expansion leads to,

$$\Delta \mathbf{z} = \mathbf{z} - \mathbf{z}_1^p = \left[\begin{pmatrix} \nabla_{\mathbf{z}} \mathcal{H}(\mathbf{z}) \\ \nabla_{\mathbf{z}} \mathcal{S}(\mathbf{z}, r)^\top \end{pmatrix}^{-1} \begin{bmatrix} \mathcal{H}(\mathbf{z}) \\ \mathcal{S}(\mathbf{z}, r) \end{bmatrix} \right]_{\mathbf{z}=\mathbf{z}_1^p} \quad (21)$$

The Newton point $\mathcal{N}(\mathbf{z})$ for approximating the solution of (21) is given by,

$$\mathcal{N}(\mathbf{z}) := \mathbf{z}_1^p + \eta \left[\begin{pmatrix} \nabla_{\mathbf{z}} \mathcal{H}(\mathbf{z}) \\ \nabla_{\mathbf{z}} \mathcal{S}(\mathbf{z}, r)^\top \end{pmatrix}^{-1} \begin{bmatrix} \mathcal{H}(\mathbf{z}) \\ \mathcal{S}(\mathbf{z}, r) \end{bmatrix} \right]_{\mathbf{z}=\mathbf{z}_1^p} \quad (22)$$

The “ η ” is Newton step size, which should be chosen to be small enough to ensure global convergence. The map $\mathcal{N}(\mathbf{z}) : \mathbb{R}^{(n+2)} \rightarrow \mathbb{R}^{(n+2)}$ is referred to as Newton map, that is iteratively applied to \mathbf{z} until a certain convergence criterion

$$\|\mathcal{N}^\kappa(\mathbf{z}) - \mathcal{N}^{\kappa-1}(\mathbf{z})\| \leq \epsilon, \quad \kappa = 1, 2, \dots \quad (23)$$

is met. In (23) ϵ denotes the desired tolerance level. Usually, the Newton method converges quadratically with a predictor point \mathbf{z}_1^p sufficiently close to \mathbf{z}_2 . If iterations fail to converge, then a step size adjustment is required.

2) Reversion Phenomenon: From Fig.3, it is clear that the sphere s_1 intersects the homotopy curve at two possible points, one in the forward direction \mathbf{z}_0 and another in the backward direction \mathbf{z}_2 . Therefore, there is still a chance that even with a predictor point \mathbf{z}_1^p in the close vicinity of a forward solution \mathbf{z}_2 , the Newton-Raphson in the corrector step can converge to a preceding solution for the system in (20). This phenomenon is known as the reversion effect or backtracking [13].

The backtracking phenomenon can be detected by evaluating the normal vector’s direction at each point of intersection. For the s_1 sphere, the following expression allows us to evaluate the directions of the normal vector,

$$\left(\cos^{-1} \left(\frac{\nabla_{\mathbf{z}} \mathcal{S}(\mathbf{z}, r)}{\|\nabla_{\mathbf{z}} \mathcal{S}(\mathbf{z}, r)\|} \right) \right)_{\mathbf{z}_0} = \left(\cos^{-1} \left(\frac{\nabla_{\mathbf{z}} \mathcal{S}(\mathbf{z}, r)}{\|\nabla_{\mathbf{z}} \mathcal{S}(\mathbf{z}, r)\|} \right) \right)_{\mathbf{z}_2} \quad (24)$$

In (24) $\nabla_{\mathbf{z}} \mathcal{S}(\mathbf{z}, r) \in \mathbb{R}^{n+2}$ is the gradient of the corrector equation (13), while \cos^{-1} function is used to find the angle with respect to each variable in the normal vector. Once the reversion is detected, a slightly perturbed predicted solution $\tilde{\mathbf{z}}_1^p$ is used as an initial guess in the corrector step by increasing the sphere’s radius by a small amount “ δr ”, resulting in a forward solution.

3) Adaptive sphere strategy: Traditionally, HCMs are reprimanded for slowness in path tracking. Hence, an adaptive sphere size strategy is devised to improve the computational speed and modify the algorithm to trace the boundary curves with sharp edges. The proposed approach is based on understanding the radius of curvature of the homotopy path. Larger the curvature flatter the curve. Contrarily, the smaller the radius of curvature steeper the curve. As the system in (11) defines a homotopy curve by the intersection of $(n+1)$ implicit hypersurfaces, the radius of curvature formula can be stated. as [18],

$$\tau = \frac{\|\dot{\mathbf{z}}(\alpha)\|^3}{\left| \left(\dot{\mathbf{z}}(\alpha)^\top \cdot \nabla_{\mathbf{z}} \dot{\mathbf{z}}(\alpha) \right)^\top \wedge \dot{\mathbf{z}}(\alpha) \right|} \quad (25)$$

Here $\dot{\mathbf{z}}(\alpha)$ is the normalized tangent vector calculated numerically through (16), while $\nabla_{\mathbf{z}} \dot{\mathbf{z}}(\alpha) \in \mathbb{R}^{(n+2) \times (n+2)}$ is the gradient of tangent vector. And operator “ \wedge ” is the wedge product. Here, we propose an asymptotic function of τ to calculate the radius of sphere r from a maximum and minimum bound,

$$r = \tanh(\tau) = \frac{\mathcal{A}e^\tau - \mathcal{B}e^{-\tau}}{C e^\tau + D e^{-\tau}} \quad (26)$$

In (26) the values of C and D are 1, while \mathcal{A} and \mathcal{B} correlates to the maximum and minimum bound on the value of the sphere’s radius, respectively. It was noted that with

the proposed methodology, the spherical path tracking scheme becomes faster and more adaptable for tracing the boundary curves with sharp turns.

C. Algorithm Implementation

A two-stage implementation is adopted to trace the solution space boundary of (1). First, a single-point solution is calculated by varying only a single parameter, i.e., λ_1 . Hence (11) becomes a set of $(n + 1)$ equations in $(n + 1)$ unknowns. To solve such a set of equations, one can use the Transversality Enforced Newton-Raphson (TENR) method from [9]. As the system in (11) consists of non-linear algebraic equations, this means one or more isolated solutions exist. Each of these isolated solutions associates with a distinct solution boundary curve. Relaxed TERN iterations are deployed to identify these various roots, later to be used as an initial starting point for tracing the corresponding solution branch.

In the next stage, the second parameter λ_2 is also free to vary; this results in an underdetermined system with $(n + 1)$ equations in $(n + 2)$ variables. Therefore, the solution of (11) becomes a 1-dimensional curve, which is traced by the proposed SC method that uses the initial point, i.e., \mathbf{z}_i from the first stage. Detailed procedure for the SC path tracking is presented in Algorithm 1.

Algorithm 1 Spherical Continuation Path Tracking

```

1: procedure PREDICTOR-CORRECTOR( $\mathbf{z}_i, r$ )
   input
2:   begin
3:    $\mathbf{z}_i \in \mathbb{R}^{n+2}$ , such that  $\mathcal{H}(\mathbf{z}_i) = 0$ ;            $\triangleright$  initial point
4:    $r > 0$ ;                                        $\triangleright$  initial sphere's radius
5:   end;
6:   repeat                                        $\triangleright$  predictor step
7:    $\mathbf{z}_i^p := \mathbf{z}_i + r \cdot \delta \mathbf{z}$ ;
8:   repeat                                        $\triangleright$  corrector step
9:    $\mathcal{N}(\mathbf{z}) := \mathbf{z}_i^p + \alpha \left[ \begin{pmatrix} \nabla_{\mathbf{z}} \mathcal{H}(\mathbf{z}) \\ \nabla_{\mathbf{z}} \mathcal{S}(\mathbf{z}, r) \end{pmatrix}^{-1} \begin{bmatrix} \mathcal{H}(\mathbf{z}) \\ \mathcal{S}(\mathbf{z}, r) \end{bmatrix} \right]_{\mathbf{z}=\mathbf{z}_i^p}$ ;
10:  until convergence;
11:   $\|\mathcal{N}^\kappa(\mathbf{z}) - \mathcal{N}^{\kappa-1}(\mathbf{z})\| \leq \epsilon$ ,  $\kappa = 1, 2, \dots$ 
12:  return  $\mathbf{z}_{i+1}$ ;                                $\triangleright$  Next point on the curve
13:  choose a new radius of sphere  $r > 0$  from (26);
14:  until traversing is stopped.
15: end procedure

```

IV. NUMERICAL RESULTS

This section presents results for two different networks. First, a small three-bus system and later an IEEE 300-bus test case to assess the proposed SC algorithm's computational performance.

A. Three Bus System

A small three bus system is shown in Figure.5, which is a slightly modified network from [4]. This network has following settings; the bus 1 is a slack bus with $\hat{V}_1 = 1.0 \angle 0^\circ$. Bus 2 is a PV bus with voltage setpoint $\hat{V}_2 = 1.0 \angle \delta_2$ and bus 3 is a PQ bus with complex voltage phasor $\hat{V}_3 = V_3 \angle \delta_3$. All the

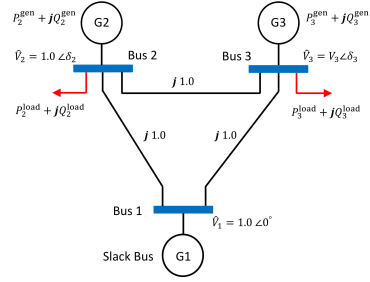


Fig. 5: Three bus network.

lines in the network are assumed to be lossless with inductance set to $X_{12} = X_{13} = X_{23} = 1.0$ (p.u.). We also assume, that the voltage magnitude at bus 3 should satisfy (7), such that $0.9 \leq |V_3| \leq 1.1$ (p.u.).

For the given network topology, the boundary manifold is confined in $P_2 - P_3 - Q_3$ space. Here, P_2 and P_3 describe active power injection at bus 2 and bus 3, respectively. While Q_3 is the reactive power injection at bus 3. Thus, the feasibility boundary is a certain surface in this 3-dimensional space. An explicit form of this surface for the given values of parameters is shown in Fig.8. We note that the shape of the surface is rather complex, even for this very simple three bus network. Next, Fig.6 illustrates the cross-sections of the surface in three different planes, namely $P_2 - P_3$, $P_2 - Q_3$, and $P_3 - Q_3$ (every time assuming fixed value of the third parameter), while Fig.7 shows the projections of the surface to the corresponding planes.

The first cross-section considers the boundary manifold in the $P_2 - P_3$ plane. The algorithmic procedure first finds a single-point solution on the $P_2 - P_3$ boundary curve for a fixed value of Q_3 . Then the proposed SC algorithm releases the second varying parameter to trace the corresponding 1-dimensional curve. For example, Fig.6a shows a slice of the boundary manifold by β^1 curve in $P_2 - P_3$ plane with $Q_3 = 0.02$ (p.u.). The projection of the manifold in $P_2 - P_3$ space is provided in Fig.7a. Each curve in Fig.7a corresponds to a particular value of Q_3 . From this projection, it is noticeable that the feasibility space boundary is bounded with inner foldings. The space within the inner folds represents the regions where different numbers of equilibria exist.

Another cross-section examines the feasibility boundary in $P_2 - Q_3$. A similar algorithmic procedure was used to compute β^2 curve (see Fig.6b) depicting the slice within the $P_2 - Q_3$ plane for $P_3 = 0.02$ (p.u.). It is apparent from Fig.6b that the β^2 curve is non-convex and also folded. The nomograms of the boundary manifold in $P_3 - Q_3$ space is given in Fig.7b for different values of P_3 . Folding within the boundary manifold is also observable from this projection.

Finally, the voltage feasibility boundary was considered in $P_2 - P_3$ space. From the previous cases, it was perceived that the solution manifold is clearly folded; hence, there is a possibility to have disconnected boundary curves. Figure.6c depicts a slice in the $P_3 - Q_3$ plane by limiting $P_2 = 0.02$ (p.u.). Two disconnected boundary curves, namely β^3 and β^4 are drawn in this slice, as shown in Fig.6c. First, the initial points were calculated corresponding to each of these curves,

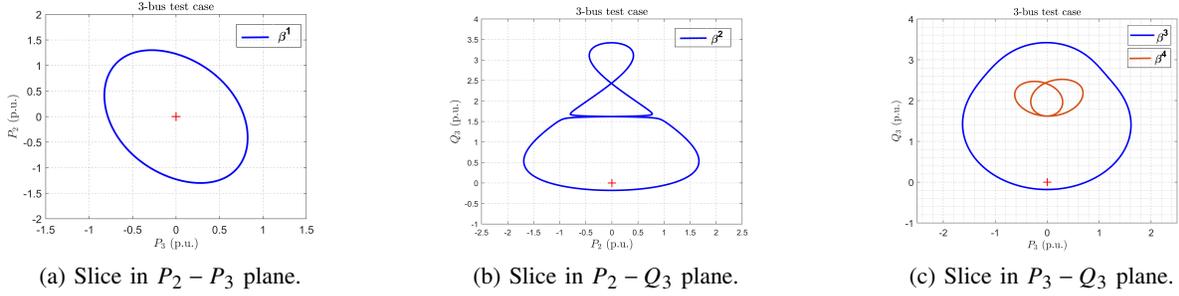
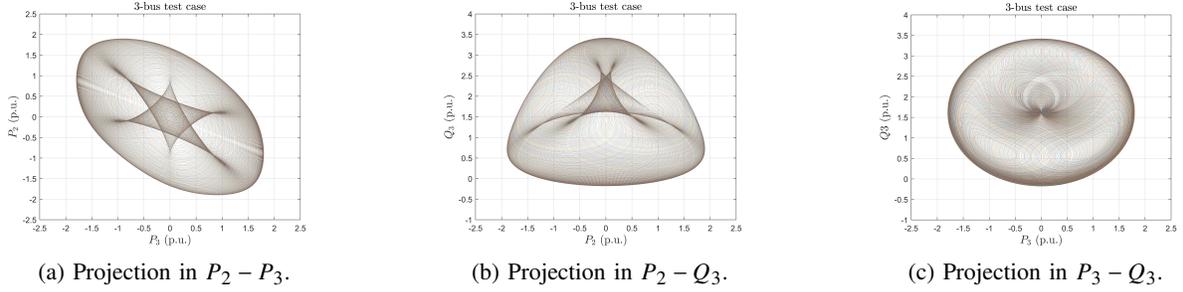
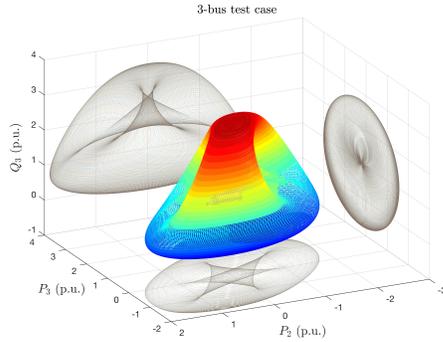
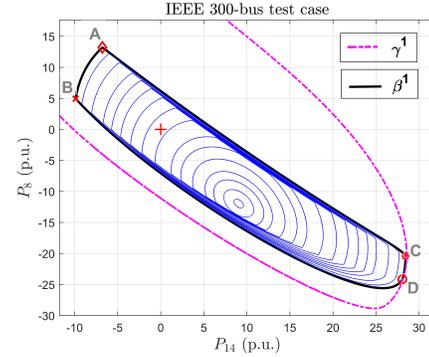


Fig. 6: Cross-sections of the voltage feasibility boundary (3-bus system).

Fig. 7: Projection of the voltage feasibility boundary in $P_2 - P_3 - Q_3$ (3-bus system).Fig. 8: Voltage feasibility boundary surface in $P_2 - P_3 - Q_3$.Fig. 9: Boundary curves in $P_8 - P_{14}$ as contours of Q_{14} .

and then, the proposed SC is initiated to trace these solution boundaries. The nomograms of feasibility boundary in $P_3 - Q_3$ space are given in Fig.7c as contours of P_2 .

The projections given in $P_2 - P_3$, $P_2 - Q_3$ and $P_3 - Q_3$ were combined to depict the 2-dimensional boundary surface in $P_2 - P_3 - Q_3$. Figure. 8 shows such surface together with all the projections. In comparison to previous works, this example describes the feasibility space boundary with the operational constraints. Furthermore, the feasibility boundary was calculated with $p = 3$, resulting in a 2-dimensional surface. From the computational context, the proposed SC method did not suffer from any numerical stability issues. The variable sphere strategy further improved the computational capabilities, enabling us to compute boundary curves faster and with non-convex sections. Although this three bus network is small, the complexity of the problem is easy to depict.

B. IEEE 300-bus Test Case

This section presents results for an IEEE 300-bus test case to evaluate the proposed SC algorithm's performance in terms of computational tractability and scalability to large networks. The 1-dimensional feasibility boundary curves for this network are shown in Fig.9. These curves present the slices of the feasibility boundary in the $P_8 - P_{14}$ plane for $0 \leq Q_{14} \leq 5.8$ (p.u.), and satisfy the voltage magnitude constraints i.e., $0.9 \leq |V_i| \leq 1.1$ (p.u.) on all the 231 load buses (thus, amounting to 462 conditions of the type (7)).

For such a large test network, calculating 1-dimensional boundary curves was a computationally burdensome task. The proposed mathematical formulation with scalar transversality condition allowed the fast computation of these curves without additional computational overhead, even with auxiliary equations representing the inequality constraints. This paper's formulation resulted in an average computational time (for calculating a single curve from Fig.9) of about 2.73 seconds.

TABLE I: Computational time for different IEEE cases.

IEEE cases	λ_1	λ_2	t_{hc} seconds	t_{sc} seconds	t_{sc}^* seconds
9 Bus	P_2	P_5	3.21	1.66	1.10
14 Bus	P_2	P_3	5.67	1.94	1.31
57 Bus	P_8	P_{10}	3.97	1.83	1.29
300 Bus	P_8	P_{14}	35.36	11.1	2.73

In contrast, the formulation from [4] resulted in 35.36 seconds, as it requires solving almost double the number of variables for each point on the boundary.

The sharp corners are visible in some of the curves from Fig.9. For instance, the β^1 curve represents the slice of the feasibility boundary in $P_8 - P_{14}$ for $Q_{14} = 0$ (p.u.). The corresponding slice of the solvability boundary (i.e., without considering voltage magnitude constraints on load buses) is given by γ^1 curve. Four different sharp turning points namely, A, B, C, D are identified on β^1 curve. These abrupt curvature changes represent the points where different operational constraints are reached. At the section A – B, A – C and B – D the power injections (i.e., P_8 and P_{14}) are bounded as the system in (1) reaches the lower limit of voltage magnitude on bus 14 and bus 282. While the section C – D coincides with the γ^1 manifesting the boundedness of the power injections, i.e., P_8 and P_{14} are due to the solvability condition of the power flow equations. The proposed SC method with adaptive sphere strategy enabled us to trace these curves faster without encountering any numerical instabilities. The traditional PC method from [4] suffered from numerical instabilities around sharp curvature changes as the hyperplane-based continuation becomes slower in the vicinity of sharp turning points, requires a precise adjustment for the continuation step size.

For the proposed algorithm, the time required to calculate 1-dimensional boundary curves was compared with the standard method from [4], and a variant of the SC method from [19] to assess the scalability towards large networks. Several runs were performed on different IEEE cases (including the 300-bus test case), and an average time is reported here. In Table.I, parameters λ_1 and λ_2 designates the pair of active power injections for which the 1-dimensional boundary curves were computed. Here t_{hc} , t_{sc} describe the time for algorithms based on the approach from [4] and [19] respectively, while t_{sc}^* delineates the computational time for the proposed SC algorithm with adaptive sphere size strategy. From Table.I it is clear that the adaptive SC method introduced in this paper surpasses the traditional approaches from [4] and [19].

V. CONCLUSIONS AND FUTURE WORK

We have introduced an adaptive Spherical Continuation (SC) method with a variable sphere strategy for calculating 1-dimensional boundary curves with computational tractability, speed, and scalability to large networks. A standardized mathematical formulation is proposed to extend the power flow feasibility problem to a particular equivalent system of the solvability problem, using the slack variable methodology. This approach converts the inequality constraints into a set of polynomial equations suitable to consider in the power flow model, thus preserving the power flow problem's sparsity

property. Here, a scalar transversality condition was used to enforce the solution of the power flow equations on the boundary of feasibility space, which allowed computing the boundary points without initialization heuristics, smaller computational overhead, and better scalability.

We show that even for a small 3-bus system, the feasibility boundary is a complex manifold with folded parts representing multiple equilibrium regions. The SC algorithm's performance was assessed on an IEEE 300-bus network, calculating 1-dimensional boundary curves faster than the existing algorithms without encountering any numerical instabilities. We also show that the SC algorithm can trace section of the curves with sharp corners or non-convexity. Future work includes using the method for potential practical applications like contingency analysis, improving local optima in relaxed OPF problems or determining an electric grid's transfer capabilities, etc.

REFERENCES

- [1] K. Morison, L. Wang, and P. Kundur, "Power system security assessment," *IEEE power and energy magazine*, vol. 2, no. 5, pp. 30–39, 2004.
- [2] V. Ajjarapu, *Computational techniques for voltage stability assessment and control*. Springer Science & Business Media, 2007.
- [3] M. Mittelstaedt, S. Bauer, and A. Schnettler, "An iterative method for determining the most probable bifurcation in large scale power systems," *IEEE Transactions on Power Systems*, vol. 32, no. 4, pp. 2966–2973, 2016.
- [4] I. A. Hiskens and R. J. Davy, "Exploring the power flow solution space boundary," *Power Systems, IEEE Transactions on*, vol. 16, no. 3, pp. 389–395, 2001.
- [5] B. C. Lesieutre and I. A. Hiskens, "Convexity of the set of feasible injections and revenue adequacy in ftr markets," *IEEE Transactions on Power Systems*, vol. 20, no. 4, pp. 1790–1798, 2005.
- [6] J. Jarjis and F. Galiana, "Quantitative analysis of steady state stability in power networks," *IEEE Transactions on Power Apparatus and Systems*, no. 1, pp. 318–326, 1981.
- [7] V. Ajjarapu and C. Christy, "The continuation power flow: a tool for steady state voltage stability analysis," *Power Systems, IEEE Transactions on*, vol. 7, no. 1, pp. 416–423, 1992.
- [8] M. E. Karystianos, N. G. Maratos, and C. D. Vournas, "Maximizing power-system loadability in the presence of multiple binding complementarity constraints," *IEEE Transactions on Circuits and Systems I: Regular Papers*, vol. 54, no. 8, pp. 1775–1787, 2007.
- [9] M. Ali, A. Dymarsky, and K. Turitsyn, "Transversality enforced newton raphson algorithm for fast calculation of maximum loadability," *IET Generation, Transmission & Distribution*, 2017.
- [10] T. Van Cutsem, "A method to compute reactive power margins with respect to voltage collapse," *IEEE Transactions on Power Systems*, vol. 6, no. 1, pp. 145–156, 1991.
- [11] B. I. Ayuev, V. V. Davydov, and P. M. Erokhin, "Fast and reliable method of searching power system marginal states," *IEEE Transactions on Power Systems*, vol. 31, no. 6, pp. 4525–4533, 2016.
- [12] S. D. Rao, D. J. Tylavsky, and Y. Feng, "Estimating the saddle-node bifurcation point of static power systems using the holomorphic embedding method," *International Journal of Electrical Power & Energy Systems*, vol. 84, pp. 1–12, 2017.
- [13] K. Yamamura, "Simple algorithms for tracing solution curves," *IEEE Transactions on Circuits and Systems I: Fundamental Theory and Applications*, vol. 40, no. 8, pp. 537–541, 1993.
- [14] S. Chandra, D. Mehta, and A. Chakraborty, "Locating power flow solution space boundaries: A numerical polynomial homotopy approach," *arXiv preprint arXiv:1704.04792*, 2017.
- [15] D. K. Molzahn, "Computing the feasible spaces of optimal power flow problems," *IEEE Transactions on Power Systems*, vol. 32, no. 6, pp. 4752–4763, 2017.
- [16] M. Ali, E. Gryazina, and K. S. Turitsyn, "Fast calculation of the transfer capability margins," in *2019 IEEE Milan PowerTech*. IEEE, 2019, pp. 1–6.
- [17] E. L. Allgower and K. Georg, *Introduction to numerical continuation methods*. SIAM, 2003.
- [18] R. Goldman, "Curvature formulas for implicit curves and surfaces," *Computer Aided Geometric Design*, vol. 22, no. 7, pp. 632–658, 2005.
- [19] G. Diaz-Arango, H. Vázquez-Leal, L. Hernandez-Martinez, M. T. S. Pascual, and M. Sandoval-Hernandez, "Homotopy path planning for terrestrial robots using spherical algorithm," *IEEE Transactions on Automation Science and Engineering*, vol. 15, no. 2, pp. 567–585, 2017.